nature portfolio

https://doi.org/10.1038/s41586-022-04746-6

Supplementary information

Axial Higgs mode detected by quantum pathway interference in RTe_3

In the format provided by the authors and unedited

Axial Higgs Mode Detected by Quantum Pathway Interference in RTe_3

Yiping Wang[1], Ioannis Petrides[2], Grant McNamara[1], Md Mofazzel Hosen[1], Shiming Lei[3], Yueh-Chun Wu[4], James L. Hart[5], Hongyan Lv[6], Jun Yan[4], Di Xiao[7,8], Judy J. Cha[5], Prineha Narang[2], Leslie M. Schoop[3], Kenneth S. Burch[1*]

[1]*Department of Physics, Boston College, Chestnut Hill, MA 02467, USA*

[2]*John A. Paulson School of Engineering and Applied Sciences, Harvard University, Cambridge, MA 02138, USA*

[3]*Department of Chemistry, Princeton University, Princeton, NJ 08544, USA*

[4]*Department of Physics,University of Massachusetts Amherst, Amherst, MA 01003 USA*

[5]*Department of Mechanical Engineering and Materials Science, Yale University, New Haven, CT 06511, USA*

[6]*Key Laboratory of Materials Physics, Institute of Solid State Physics, HFIPS, Chinese Academy of Sciences, Hefei 230031, China*

[7]*Department of Materials Science and Engineering, University of Washington, seattle, WA 98105, USA*

[8]*Department of Physics, University of Washington, seattle, WA 98105, USA*

[*] *To whom correspondence should be addressed; E-mail: ks.burch@bc.edu*

Tranmission Electron Microscopy For TEM analysis, $GdTe_3$ was exfoliated onto SiO_2 / Si substrates in a glove box (Ar environment) using the scotch tape method. $GdTe_3$ flakes were transferred to the TEM grid (Quantfoil) by first laying the grid directly onto the substrate, placing a droplet of IPA onto the grid, and allowing the IPA to evaporate, thereby ensuring good contact between the grid and substrate. A 20 mL drop of 10% hydrofluoric acid (HF) was then placed onto the grid / substrate, and immediately after the grid was washed in DI water. In total, the flakes were exposed to ambient atmosphere for 3 minutes, including the HF etch step and transfer to the TEM. Electron imaging and diffraction was performed in a FEI Tecnai Osiris operated at 200 kV.

For the flake characterized in Fig. S1a,b, we observe a single q vector, which is aligned vertically in Fig. S1b. For the flake characterized in Fig. S1c,d, scattering to two orthogonal q vectors are observed; however, scattering to the vertical q vector (see Fig. S1d) is substantially stronger (10×) than scattering to the horizontal q vector. This data indicates that exfoliated flakes either consist of single CDW domains, or that their CDW domain structure is dominated by one domain type, and may thus be approximated as single domain.

Group theory of phonon Raman tensor Given the space group symmetry of the bulk, undistorted RTe_3 is bmbm (point group is D2h), we expect 12 Raman active phonons: 4Ag + 8Bg. Group theory predicts the Raman response tensor of Ag and Bg to be the following:

$$Ag = \begin{pmatrix} a & 0 & 0 \\ 0 & b & 0 \\ 0 & 0 & c \end{pmatrix}; Bg = \begin{pmatrix} 0 & d & 0 \\ d & 0 & 0 \\ 0 & 0 & 0 \end{pmatrix}$$

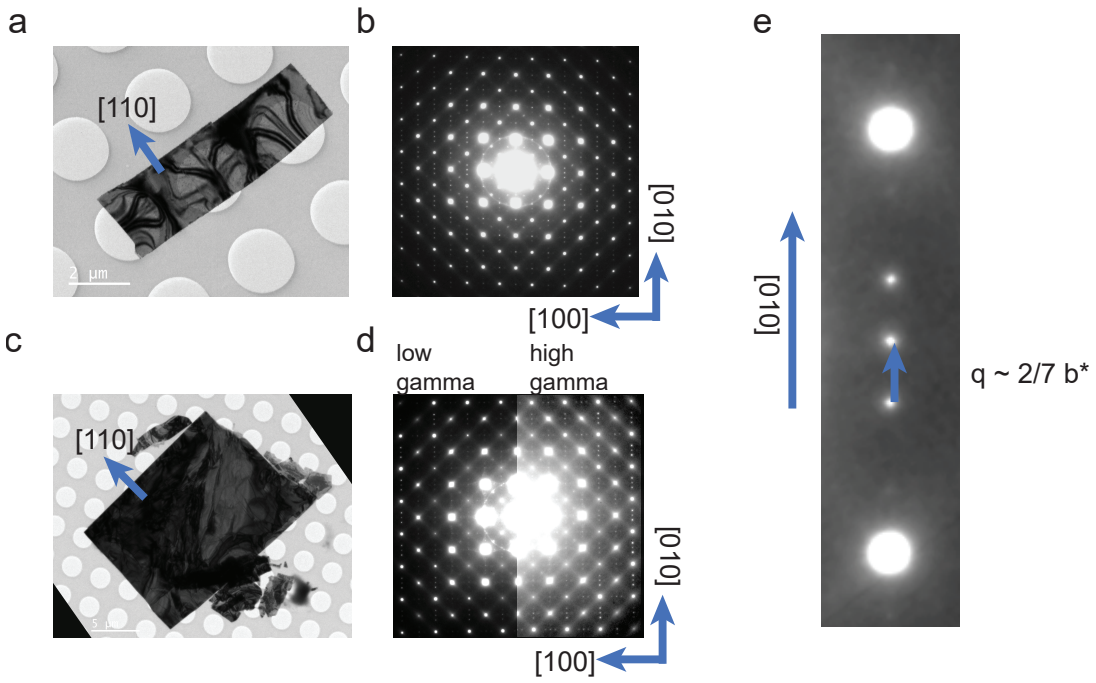

Figure S1: TEM results. (a) Low magnification bright field TEM image of $GdTe_3$ flake 1. (b) Electron diffraction pattern of flake 1. (c) Low magnification bright field TEM image of $GdTe_3$ flake 2. (d) Electron diffraction pattern of flake 2. (e) CDW vector length

where a, b, c, d are independent coefficients. These matrices are written in a coordinate system where the tensor's x and y axes are parallel to the crystallographic a and b axes. For the Ag phonon mode, the Raman tensor contains two diagonal terms and for the Bg phonon mode, the Raman tensor contains two same off diagonal terms. The Raman intensities can be represented as:

$$I = |\langle e_i| R |e_f\rangle|^2$$

37 The selection rules allow for both Ag and Bg phonons to be measured for light polarized in

the ab plane and they can be measured simultaneously in both crossed and parallel polarization configurations.

According to group theory, we calculated the predicted angular dependence of the Raman response in the backscattering geometry in Fig. S2. For both Ag and Bg phonons are expected to show 2 or 4 fold modulated intensities in parallel polarization channel and show 4 fold modulated intensities in cross polarization channel. This result is consistent with the fitting in Fig. 3 and 4 in the main text.

Image of RTe_3 flakes for Raman scattering As shown in Supplemental Fig .S1A and c the sharp edges of the exfoliated crystal align with the [101] direction. The edges are perpendicular (i.e. ninety degrees) to each other. This is consistent with a natural cleavage of the Te layers. In Supplemental Fig. S2 we show the optical image of $GdTe_3$ and $LaTe_3$ flakes we used in our Raman measurement. We specifically choose exfoliation flakes with sharp edges separated by ninety degrees, this allows us to pre-identify the crystal axes of the RTe_3 flakes.

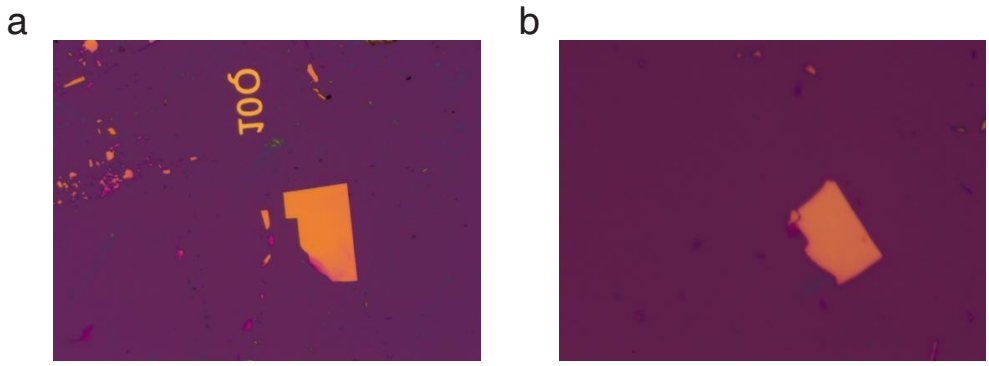

Figure S2: Optical image. (a) Optical image of $GdTe_3$ flake on SiO_2/Si. (b) Optical image of $LaTe_3$ flake on SiO_2/Si.

$LaTe_3$ representative spectra We present representative spectra of $LaTe_3$ in Fig. S3. We showed both angular dependent spectra and temperature dependent spectra. As the CDW transition temperature is much higher than $GdTe_3$, the CDW mode energy is also lower.

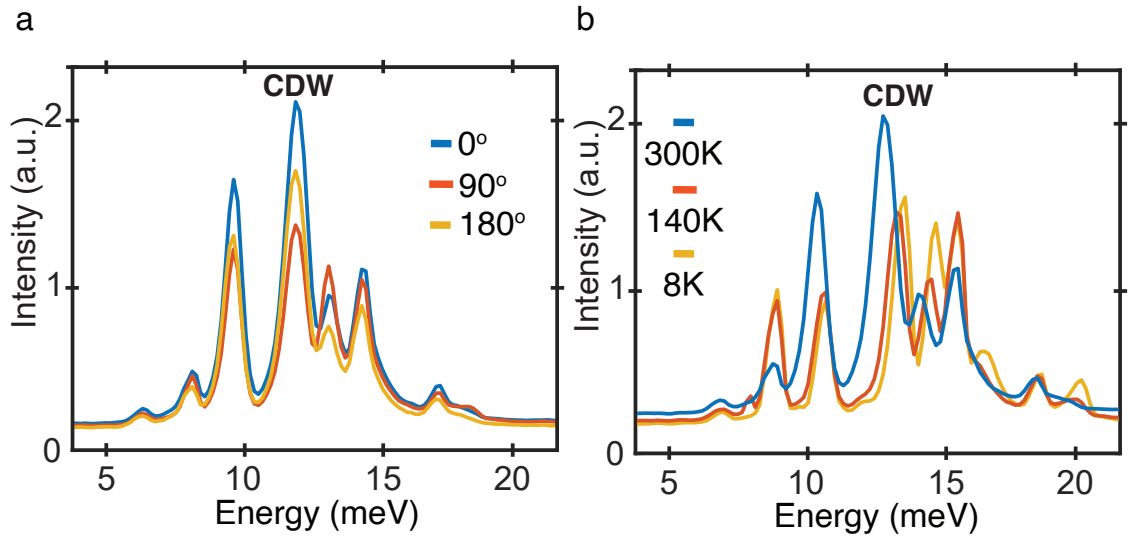

Figure S3: (a) $LaTe_3$ representative polarization angle dependent spectra in parallel polarization. (b) $LaTe_3$ representative temperature dependent spectra in parallel polarization.

Data Fitting Details To accurately determine the phonon and Higgs mode frequencies, we fit the Raman spectra with the Voigt function

$$I(\omega, \sigma, \Gamma, A) = \int_{-\infty}^{\infty} G(\omega', \sigma) L(\omega - \omega', \Gamma, A) d\omega'$$

which is a convolution of a Gaussian and a Lorentzian function. Here the Lorentzian represents a phonon mode and we use a Gaussian to account for the instrumental resolution. The Gaussian width σ = 1 cm^{-1} is determined by the central Rayleigh peak. Γ is the phonon width and A is phonon amplitude. We show the fitting results in Fig. S4. We use Voigt function to fit 3 independent spectra and then take the squared 2-norm of the residual as: error = $\sum[fun(\theta) -$

$\chi(\theta)]^2$. Our error is the square root of this summation for each peak.

Following the Voigt fittings, the phonon amplitude values versus the rotation of the crystal (θ) are extracted to analyze their angular dependence. We constructed polar plots for individual angular dependent modes of Raman spectra in both parallel and cross linear polarization and fitted them accordingly to their particular Raman tensors.

Crossed and parallel polarization configurations for a given phonon are analyzed and fitted simultaneously with the susceptibility model from different Raman tensors.

$$XX = \begin{pmatrix} 1 & 0 & 0 \end{pmatrix} \cdot U^T \cdot R \cdot U \cdot \begin{pmatrix} 1 \\ 0 \\ 0 \end{pmatrix}$$

$$XY = \begin{pmatrix} 1 & 0 & 0 \end{pmatrix} \cdot U^T \cdot R \cdot U \cdot \begin{pmatrix} 0 \\ 1 \\ 0 \end{pmatrix}$$

where R is the Raman tensor, U is the rotation matrix, and U^T is the transpose of this rotation matrix. For polar fitting purposes, Ag, CDW, Bg tensors and U are defined as follows:

$$CDW = \begin{pmatrix} e & d & 0 \\ -d & f & 0 \\ 0 & 0 & g \end{pmatrix}$$

$$Ag = \begin{pmatrix} e & 0 & 0 \\ 0 & f & 0 \\ 0 & 0 & g \end{pmatrix}$$

$$Bg = \begin{pmatrix} 0 & d & 0 \\ d & 0 & 0 \\ 0 & 0 & 0 \end{pmatrix}$$

$$U = \begin{pmatrix} \cos[\theta] & -\sin[\theta] & 0 \\ \sin[\theta] & \cos[\theta] & 0 \\ 0 & 0 & 1 \end{pmatrix}$$

Where d,e and f are independent Raman tensor coefficients, Fitting parameters e and f are diagonal Raman tensor terms that are not necessarily equal, while d is the off-diagonal component that is necessarily equal in both instances it appears for any given Raman tensor. In the x-y plane, these tensors directly correspond to theory as shown in Fig. S5.

We square the resulting functions $I = | < e_i|U^T \cdot U \cdot U|e_f > |^2$ in the case of Ag and Bg phonons and CDW Higgs mode to represent Raman intensities. A representative angular fitting for both XX and XY is in Fig. S5. These results are consistent with the data fitting in main text Fig. 3 and 4. Especially, the CDW Higgs mode shows 2 fold symmetry in both parallel and cross polarizations.

CDW model function (Parallel Polarization) =

$$(\cos[\theta] \cdot ((e\cos[\theta]) + (d\sin[\theta])) + \sin[\theta] \cdot ((-d\cos[\theta]) + (f\sin[\theta])))^2$$

CDW model function (Crossed Polarization) =

$$(-\sin[\theta] \cdot ((e\cos[\theta]) + (d\sin[\theta])) + \cos[\theta] \cdot ((-d\cos[\theta]) + (f\sin[\theta])))^2$$

Ag model function (Parallel Polarization) =

$$(\cos[\theta] \cdot ((e\cos[\theta])) + \sin[\theta] \cdot ((f\sin[\theta])))^2$$

Ag model function (Crossed Polarization) =

$$(-\sin[\theta] \cdot ((e\cos[\theta])) + \cos[\theta] \cdot ((f\sin[\theta])))^2$$

Bg model function (Parallel Polarization) =

$$(2d\cos[\theta]\sin[\theta])^2$$

Bg model function (Cross Polarization) =

$$((d\cos^2[\theta]) - (d\sin^2[\theta]))^2$$

This leaves us with 2 fitting parameters for Ag phonons and Higgs mode (e, f) and 1 fitting parameter for Bg phonons (d). For Raman tensor data fitting purposes depicting symmetries of

these modes, we fit the Raman susceptibility data calculated from Raman intensity as a function of polarization angle data from 0 to 360 degrees(θ) for different Raman tensor. The provided model functions above are the objective equations, which is accompanied by an initial guess for the Raman tensor function parameters. Our polar plots are fit with these parameters accordingly and simultaneously for a given phonon in both crossed and parallel polarizations to produce one set of optimized tensor parameters for the phonon that adequately fits both polarizations' model functions in accordance with input data. Fitted Raman tensor terms are input into these model functions, resulting in a fitted polar curve for each respective phonon in both crossed and parallel polarizations.

We show the theory prediction of the angular dependent symmetries in Fig. S5(a-c), and our fitted results for each mode's Raman tensor are shown in Table S1, which in turn produce our polar plot fits for each mode as shown in Fig. S6 (note mode 4 is not included as it's contribution is negligible). We also use the CDW tensor to fit the XX and XY polarization angular dependent CDW intensities in Fig. S6. As shown in Fig. S6, other than CDW mode, there are two more modes that have 2-fold polarization dependence in XY channel. These two modes disappeared above the CDW transition temperature[1]. In addition, similar to other Raman experiments[2,3] , we observe clear avoided crossing between these modes and the Higgs mode. Even in X-Ray scattering[4], the Higgs mode is strongly mixed with these phonons.

As for other phonons modes at 7.7 meV, 9.3 meV and 9.9 meV, they show Bg symmetry from their angular dependence of the Raman susceptibility (shown in Fig. S6) in XY polarization. As such they cannot couple with the Higgs mode. A close examination of Fig S6, reveals the XX angular dependence for the for the 7.9, 9.3, 9.9 and 15.9 meV phonon modes is not consistent with pure Bg symmetry. Upon further examination we have concluded the spectra

are the result of accidental or near degeneracies of Ag and Bg modes. This is most easily seen in the 15.9 meV mode. Indeed, the XX data appeared to have a 4 fold component on top of an angle independent component. This is consistent with two modes, one of Bg (four fold) and one of Ag symmetry with identical diagonal terms in the Raman tensor. In Fig. S7, we demonstrate this by plotting response upon subtracting the 0 degree data, where the Bg component is zero. A second mode is clearly observed, consistent with two nearly degenerate modes.

To systematically demonstrate this mode is actually two nearly degenerate phonons, we fit the difference spectra: $\chi(15.9meV, \theta)$- $\chi(15.9meV, 0)$ to extract the angular dependent mode paramaters for the Bg phonon. Next we fixed the Bg parameters and added a second mode to fit the original spectra at every angle. As shown in Fig. S7, when added together the modes perfectly fit the spectra. Furthermore they reveal the expected behavior, namely a perfect four fold symmetry (Bg) and angle independent response (Ag) in XX. In addition, we found that the two modes are nearly degenerate (0.2 meV apart), as expected. Turning to the modes at 7.9 meV and 9.9 meV, we found that these appear to have an accidental degeneracy between one Ag and one Bg phonon. With this in mind, we first fit the XY intensity to a purely Bg mode. Next we simultaneously fit the XY and XX data using the Bg phonon combined with an Ag mode. The Bg mode parameters were kept fixed, while the Ag where allowed to vary. The results are shown in Fig. S7 in which a clear Ag component emerges in XX which proves considerably weaker in XY under the same tensor fitting parameters, explaining our nearly perfect 4-fold symmetry originally found in XY at 7.9 and 9.9 meV. We find these fits of degenerate modes perfectly describe the data.

In addition the signal for the mode at 9.3 meV is fairly weak and it strongly overlaps with the Higgs mode. This is shown in Fig. S8 which contains the individual fits of all low enegy

modes in XX polarization. This makes is quite difficult to separate the response of this mode from the Higgs, producing an apparent anomalous angular dependence in XX.

As a last note, one may be concerned about the number of modes as compared to what is expected from group theory. Since two of the phonon modes are folded by the CDW (7.4 meV and 10.7 showing two fold in XY as well), these are not to be counted in the prediction from group theory (4 Ag modes and 8 Bg modes). However upon removing the two modes, we are now left with only 1 Ag mode and 8 Bg modes (taking into account the assumption that mode 5 was too weak to discern clear symmetry and is to be considered Bg). If we include the three new modes that are accidentally or nearly degenerate (i.e. the Ag modes at 7.9meV, 9.9 meV and 15.9 meV), we now fully account for all modes expected with the proper symmetry. This lends additional strength to our argument that the apparent discrepancies are due to accidental or near degeneracies. Specifically that the angular dependent intensity results from two modes of different symmetries.

mode	Energy (300K, meV)	Symmetry	Above T_{CDW} (Y/N)	Raman tensor
1(CDW)	5.6	2-fold	N	$\begin{pmatrix} 225 & 55 \\ -55 & 326 \end{pmatrix}$
2	7.4	2-fold	N	$\begin{pmatrix} 19 & 5 \\ -5 & 26 \end{pmatrix}$
3	7.9	B_g	Y	$\begin{pmatrix} 0 & 25 \\ 25 & 0 \end{pmatrix}$

4	7.9	A_g	Y	$\begin{pmatrix} 63 & 0 \\ 0 & 54 \end{pmatrix}$
5	8.4	NA	NA	NA
6	9.3	B_g	N	$\begin{pmatrix} 0 & 60 \\ 60 & 0 \end{pmatrix}$
7	9.9	B_g	N	$\begin{pmatrix} 0 & 46 \\ 46 & 0 \end{pmatrix}$
8	9.9	A_g	N	$\begin{pmatrix} 79 & 0 \\ 0 & 37 \end{pmatrix}$
9	10.7	2-fold	N	$\begin{pmatrix} 102 & 53 \\ -53 & 117 \end{pmatrix}$
10	11.5	A_g	Y	$\begin{pmatrix} 67 & 0 \\ 0 & -84 \end{pmatrix}$

11	12.8	B_g	N	$\begin{pmatrix} 0 & 48 \\ 48 & 0 \end{pmatrix}$
12	14.5	B_g	Y	$\begin{pmatrix} 0 & 116 \\ 116 & 0 \end{pmatrix}$
13	15.9	A_g	Y	$\begin{pmatrix} 95 & 0 \\ 0 & 95 \end{pmatrix}$
14	16.1	B_g	Y	$\begin{pmatrix} 0 & 52 \\ 52 & 0 \end{pmatrix}$
15	17.6	B_g	Y	$\begin{pmatrix} 0 & 82 \\ 82 & 0 \end{pmatrix}$

Table 1: CDW Higgs mode and Phonon fit results. The energy, symmetry(Raman polarization dependence), existence above T_{CDW} and fitted Raman tensor are listed for each Raman mode. Intensity of mode 4 is very low so the symmetry and fitted tensor is not available.

134 5

Raman Temperature and Laser Induced Heating minimization For Raman scattering, the Stokes intensity can be represented as the product of Raman susceptibility and Boltzmann factor n_B+1. While the anti-Stokes intensity can be represented as the product of Raman susceptibility and Boltzmann factor n_B.

$$I_S(\omega_0, T) = \chi * (n_B + 1) \tag{1}$$

$$I_{AS}(\omega_0, T) = \chi * n_B \tag{2}$$

Thus, the ratio of the Stokes and anti-Stokes intensity should be:

$$\frac{I_S(\omega_0, T)}{I_{AS}(\omega_0, T)} = \frac{(1 + n_B(\omega_0, T))}{(n_B(\omega_0, T))} = \frac{1 + (e^{\frac{\hbar\omega_0}{2k_BT}} - 1)^{-1}}{(e^{\frac{\hbar\omega_0}{2k_BT}} - 1)^{-1}} = e^{\frac{\hbar\omega_0}{k_BT}} \tag{3}$$

135 Via the Stokes and anti-Stokes ratio, one can get the real sample temperature sample to check
136 for laser induced heating. In our measurement, we used the 30 μ W laser power to minimize
137 the laser heating and guarantee the signal level at the same time. As shown in Fig. S9, we

plot the susceptibilities of Stokes signal ($I_S/(n_B+1)$) and anti-Stokes ($I_{AS}/(n_B)$). For the high energy phonons, the perfect overlap of the susceptibilities suggests our measurement is all in detailed balance and there's no laser heating. For the low temperature measurement, there exists obvious difference between Stokes and anti-Stokes susceptibility at low scattering energy rang(5- 10 meV). This difference is because of the resonance at the anti-Stokes side, which enhanced the enti-Stokes intensity. However, the sample is still in detailed balance and there's no laser heating show up in our measurement.

Sample with multi-domains In some of the samples we measured, we observed multi-domain CDW signal. This is consistent with the secondary CDW showed in TEM results. Different domains can result in different polarization dependence of the CDW Higgs mode. The two-fold angular dependent showed in the main text is from the samples with single domain. We present muti-domain CDW Higgs mode angular dependent polarplot here in Fig. S10.

Model for the Raman susceptibility from the Amplitude Mode Here we calculate the Raman susceptibility for the RTe electronic structure in the presence of a CDW with characteristic momentum $\boldsymbol{q}_{CDW}$ and an amplitude mode (AM) with excitation frequency ω_0. The single particle momentum space Hamiltonian in the basis of P_X and P_Y orbitals, shown in Fig. 1b, is given by

$$H(\boldsymbol{k}) = \sum_{\boldsymbol{k},i,j} \left(\mu\delta_{ij} + \epsilon^{ij}_{\boldsymbol{k}}\right) c^{\dagger}_{\boldsymbol{k},i} c_{\boldsymbol{k},j} \tag{4}$$

where

$$\begin{aligned} \epsilon^{11}_{\boldsymbol{k}} &= -2t_1\cos(k_x) - 2t_2\cos(k_y) - 4t_3\cos(k_x)\cos(k_y)\,, \\ \epsilon^{22}_{\boldsymbol{k}} &= -2t_2\cos(k_x) - 2t_1\cos(k_y) - 4t_3\cos(k_x)\cos(k_y)\,, \\ \epsilon^{12}_{\boldsymbol{k}} &= -4t_4\sin(k_x)\sin(k_y)\,, \end{aligned} \tag{5}$$

with t_1, t_2, t_3, t_4 the hopping amplitudes up to next-nearest neighbour interaction and μ the Fermi energy. The orbital overlaps define a representative hierarchy of the hopping parameters where $|t_1| \gg |t_2|, |t_3|, |t_4|$, while the electronic filling factor of the crystal results in a nonzero μ. The eigenvalues of the Hamiltonian are given by

$$\epsilon^{\pm} = \mu + \frac{1}{2}\left(\epsilon^{11}_{\boldsymbol{k}} + \epsilon^{22}_{\boldsymbol{k}} \pm \sqrt{(\epsilon^{11}_{\boldsymbol{k}} - \epsilon^{22}_{\boldsymbol{k}})^2 + 4(\epsilon^{12}_{\boldsymbol{k}})^2}\right) \tag{6}$$

In the chosen unit cell of Fig.1c, the spectrum has four eigenvalues corresponding to linear superpositions of either P_X or P_Y orbitals in the limit of vanishing next-nearest neighbor interaction, while for finite values mixing between the states occurs only at isolated regions around four points $\delta(k_x \pm \pi/2)\delta(k_y \pm \pi/2)$.

As shown in Fig. 1c, the Fermi surface of the system in the absence of the CDW can be parameterized by the lines $l_X = \delta(k_x \pm \pi/2)$ and $l_Y = \delta(k_y \pm \pi/2)$ corresponding to the positions where the nesting vector q_{CDW} connects equivalent orbitals. Additionally, there are two points $p = \delta(k_x \pm \pi/2)\delta(k_y \mp \pi/2)$ where the nesting vector $b^* - q_{CDW}$ connects orbitals with different polarization. First, we focus on the regions in the Fermi surface away from these points and assume minimal orbital mixing. In this case, the approximate Green's function characterizing each line is given in the Nambu-Gorkov basis $\psi_{\boldsymbol{k}} = \{c_{\boldsymbol{k}-\boldsymbol{q}_{CDW}/2,j}, c_{\boldsymbol{k}+\boldsymbol{q}_{CDW}/2,j}\}$, with $j = P_X$ or P_Y, as

$$G(\omega + i\delta) = [(\omega + i\delta)\sigma_0 - \xi_k\sigma_3 - \Delta\sigma_1]^{-1} \tag{7}$$

where $\xi_k = v_F k$ is the linearized energy along the momentum k perpendicular to the chosen line and $v_F(\mu)$ is the Fermi velocity defined by the Fermi energy.

The amplitude mode can be included in the dynamics using the interaction Hamiltonian $H_{int} = (b + b^\dagger)\psi^\dagger_{\boldsymbol{k}}\sigma_1\psi_{\boldsymbol{k}}$ as it couples directly to the CDW gap [5]. Here, we assume that the

operators b and $b^\dagger$ are bosonic with single particle energy $H_b = \omega_0 b^\dagger b$ and unperturbed Green's function given by $D_0(\omega) = \frac{\omega_0^2}{\omega^2 - \omega_0^2}$.

The transition probability between two states accompanied by the emission of a bosonic mode can be obtained diagramatically using Feynmann's rules. More details about the formalism can be found in standard quantum field theory textbooks [6], as well as in applications to amplitude modes in CDW systems [7,8], and phonons in semiconductors [9]. We focus on resonant processes in the limit of zero momentum transfer where an initial state of a photon with laser frequency ω_{in} is scattered to a final state of a photon with frequency $\omega_{\text{in}} + \omega$ plus an AM with frequency $-\omega$. The relevant leading order scattering amplitudes for such a process, see Fig. S11(a), are given by

$$\mathcal{M}^1_{\mu\nu}(\omega_{\text{in}}, \omega_{\text{out}}) = \int_{\omega, \boldsymbol{k}} d\omega d^2k \text{Tr} G(\omega) \gamma^\mu G(\omega + \omega_{\text{in}}) \tau G(\omega + \omega_{\text{out}}) \gamma^\nu \tag{8}$$

$$\mathcal{M}^2_{\mu\nu}(\omega_{\text{in}}, \omega_{\text{out}}) = \int_{\omega, \boldsymbol{k}} d\omega d^2k \text{Tr} G(\omega) \gamma^\mu G(\omega + \omega_{\text{in}}) \gamma^\nu G(\omega + \omega_{\text{out}}) \tau \tag{9}$$

where $\gamma^\mu = \frac{\partial \epsilon^{jj}_{\boldsymbol{k}}}{\partial k_\mu} \sigma_3$ ($j = 1$ or 2 depending on the region of Fermi surface being described) corresponds to the current vertex and defines the polarization of the emitted photon. Scattering due to the AM is determined through the interaction Hamiltonian as $\tau = \sigma_1$ (for simplicity the coupling constant is omitted).

The integrands of the two scattering amplitudes generally have three poles in the upper half of the complex plane at $\sqrt{\xi^2 + \Delta^2}$, $\sqrt{\xi^2 + \Delta^2} - \omega_{\text{in}}$ and $\sqrt{\xi^2 + \Delta^2} - \omega_{\text{out}}$. We evaluate the frequency integral using complex analysis and the residue theorem, leading to a sum of three terms where the remaining momentum integral is performed numerically. The total probability rate of the transition calculated within Fermi's Golden rule – dubbed the Raman susceptibility

– is directly proportional to

$$\chi_{\mu\nu}(\omega) \sim |\mathcal{M}_{\mu\nu}(\omega_{\text{in}}, \omega_{\text{in}} + \omega)|^2 D_0(\omega)\,, \tag{10}$$

where $\mathcal{M}_{\mu\nu} = \mathcal{M}^1_{\mu\nu} + \mathcal{M}^2_{\mu\nu}$ is the sum of scattering amplitudes.

Using the Green's function of Eq. 7 the calculated Raman susceptibility contributes equally to co-linear polarizations and is peak at the energy of the amplitude mode. This is due to the fact that our system is in fact nearly square in the ab-plane with slight orthorhombic distortion in the direction of the CDW. On the other hand, processes involving a change of polarization vanish along the Fermi lines l_X and l_Y (i.e., away from points p) because the vertices γ^μ approximate to zero when the polarization of the photon is parallel to the Fermi line being described.

We now focus on the regions around the points p in the Brillouin zone. Since orbital mixing is the strongest at these points we adopt the effective low energy Hamiltonian, see Fig. S11(b),

$$H_p(\boldsymbol{k}) = \begin{pmatrix} \xi^1_{\boldsymbol{k}} & \Delta & 0 & 0 \\ \Delta & \xi^2_{\boldsymbol{k}} & 0 & 0 \\ 0 & 0 & -\xi^1_{\boldsymbol{k}} & \Delta \\ 0 & 0 & \Delta & -\xi^2_{\boldsymbol{k}} \end{pmatrix} \tag{11}$$

where now $\xi^1_{\boldsymbol{k}} = v_1 k$ and $\xi^2_{\boldsymbol{k}} = -v_2 k$ are the linearized eigenvalues of Eq. (4) and Δ is the coupling due to the CDW. The linearized Hamiltonian depends on a single quasimomentum $k = k_x + k_y$. The numerical values of v_1 and v_2 are determined by the Fermi energy μ while their difference $|v_1 - v_2|$ by the strength of the orbital mixing parameter t_4. We note that the degeneracy at the point p is lifted due to next-nearest neighbour interaction, hence, the CDW only couples states that are connected by $q_{CDW} - b^*$, see Fig. S11(b).

The Raman susceptibility of Eq. 10 is now defined with respect to the electronic Green's function $G(\omega + i\delta) = [(\omega + i\delta) - H_p]^{-1}$, the current vertices $\gamma_\mu = \text{diag}(\gamma_\mu^+, \gamma_\mu^-, -\gamma_\mu^+, -\gamma_\mu^-)$ with $\gamma_\mu^\pm = \frac{\partial \epsilon^\pm}{\partial k_\mu}$, and, amplitude mode vertex $\tau = \sigma_0 \otimes \sigma_1$. We note that the current vertices are determined by the Fermi energy μ and the hopping parameters. Fig. S11(c) shows the calculated Raman spectra for the cross-polarization configuration in the presence of a CDW and amplitude mode. We find that resonant Raman transitions have an asymmetric nature depending on the mixing terms t_3 and t_4, as well as the Fermi energy μ that ultimately defines the nesting vector q_{CDW}. This theoretical analysis supports the experimental results and illuminates the important mechanisms by which the Higg's mode couples orbitals with different angular momentum.

1. Eiter, H.-M. *et al.* Alternative route to charge density wave formation in multiband systems. *Proceedings of the National Academy of Sciences* **110**, 64–69 (2013).

2. Lavagnini, M. *et al.* Raman scattering evidence for a cascade evolution of the charge-density-wave collective amplitude mode. *Phys. Rev. B* **81**, 081101 (2010).

3. Chen, Y. *et al.* Raman spectra and dimensional effect on the charge density wave transition in gdte3. *Applied Physics Letters* **115**, 151905 (2019).

4. Maschek, M. *et al.* Competing soft phonon modes at the charge-density-wave transitions in $DyTe_3$. *Phys. Rev. B* **98**, 094304 (2018).

5. Littlewood, P. B. & Varma, C. M. Gauge-invariant theory of the dynamical interaction of charge density waves and superconductivity. *Phys. Rev. Lett.* **47**, 811–814 (1981).

6. Peskin, M. E. & Schroeder, D. V. *An Introduction to Quantum Field Theory* (Westview Press, 1995). Reading, USA: Addison-Wesley (1995) 842 p.

7. Horovitz, B., Vardeny, Z., Ehrenfreund, E. & Brafman, O. Raman scattering from charge-density waves and application to polyacetylene. *Journal of Physics C: Solid State Physics* **19**, 7291–7305 (1986).

8. Klein, M. V. Theory of raman scattering from charge-density-wave phonons. *Phys. Rev. B* **25**, 7192–7208 (1982).

9. Reichardt, S. & Wirtz, L. Raman spectroscopy of grpahene. *Optical Properties of Graphene* (2017).

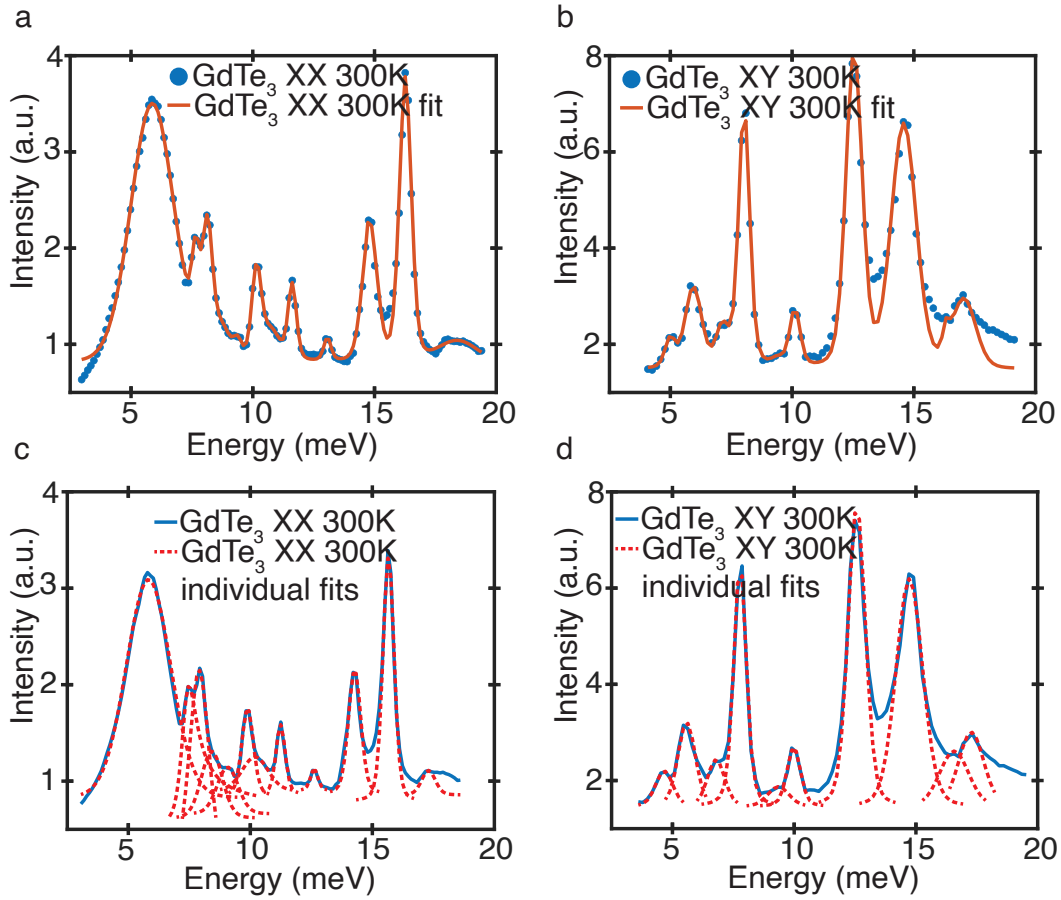

Figure S4: **Multi-Voigt data fittings** (a-b) Voigt fit results for XX (left) and XY (right) polarizations at 300K. Blue dot is the Raman spectra and red sold line is the total fitting. (c-d) show the individual peak fit of XX and XY polarization, Blue dot is the Raman spectra and red dash line is the individual peak fitting.

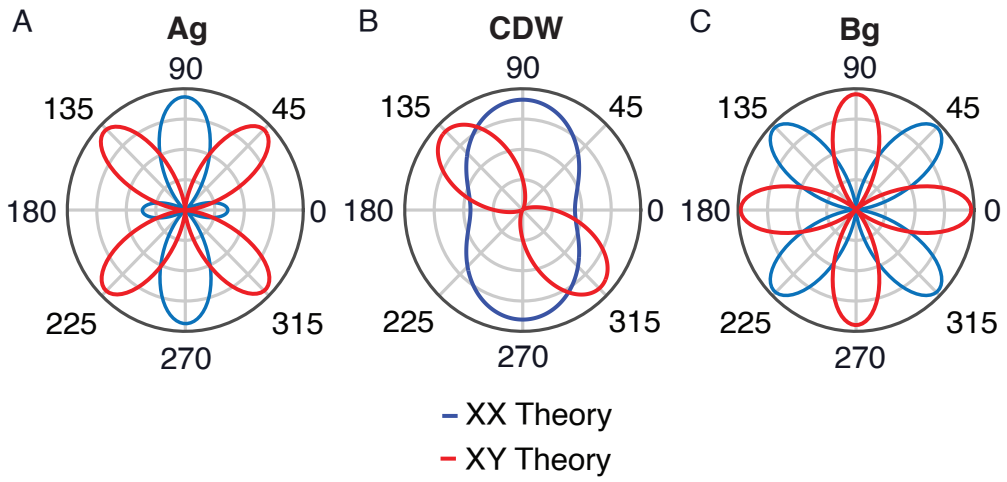

Figure S5: (a-c) Possible polar plots according to theory for Ag (a,b) and Bg (c) modes for RTe_3 using respective model functions.

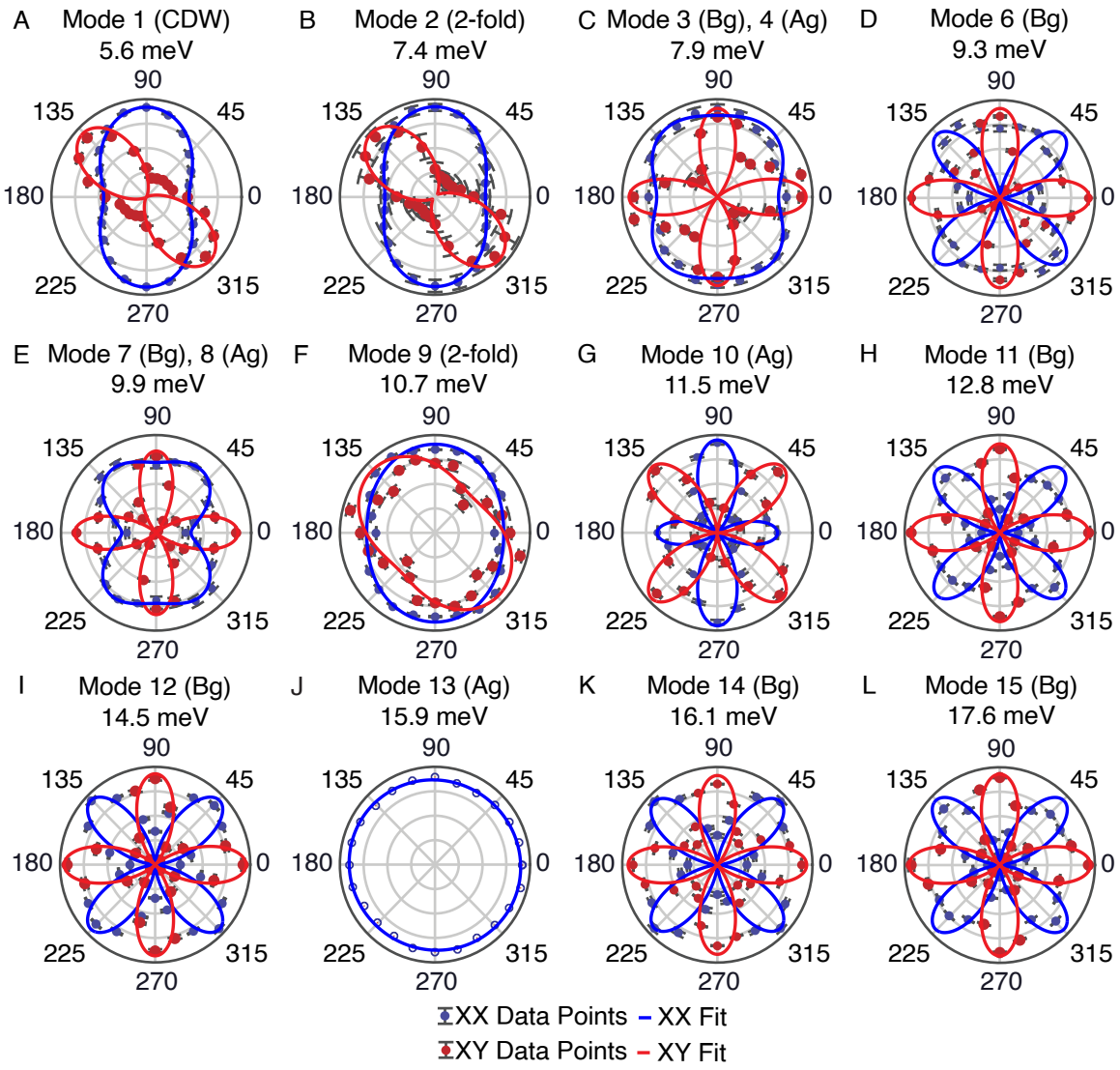

Figure S6: Experimental modes and polar fits for each $GdTe_3$ (532nm incident wavelength) mode at 300K using respective model functions (CDW, Ag, Bg). Mode 5 is excluded as the signal is too weak to accurately determine its' angle dependence. Note mode 13 (Ag) is zero in cross-polarization and therefore is not shown. Also note that modes 3 & 4 and 7 & 8 are overlapping accidental and degenerate modes consisting of an Ag and a Bg mode each, the sum of which is plotted and fitted (see fig. S7 for individual Ag and Bg fits from these modes). Fits were done using same Raman tensor fitting parameters in XX and XY in corresponding model functions for Raman tensors in XX (blue) and XY (red) polarizations, respectively.

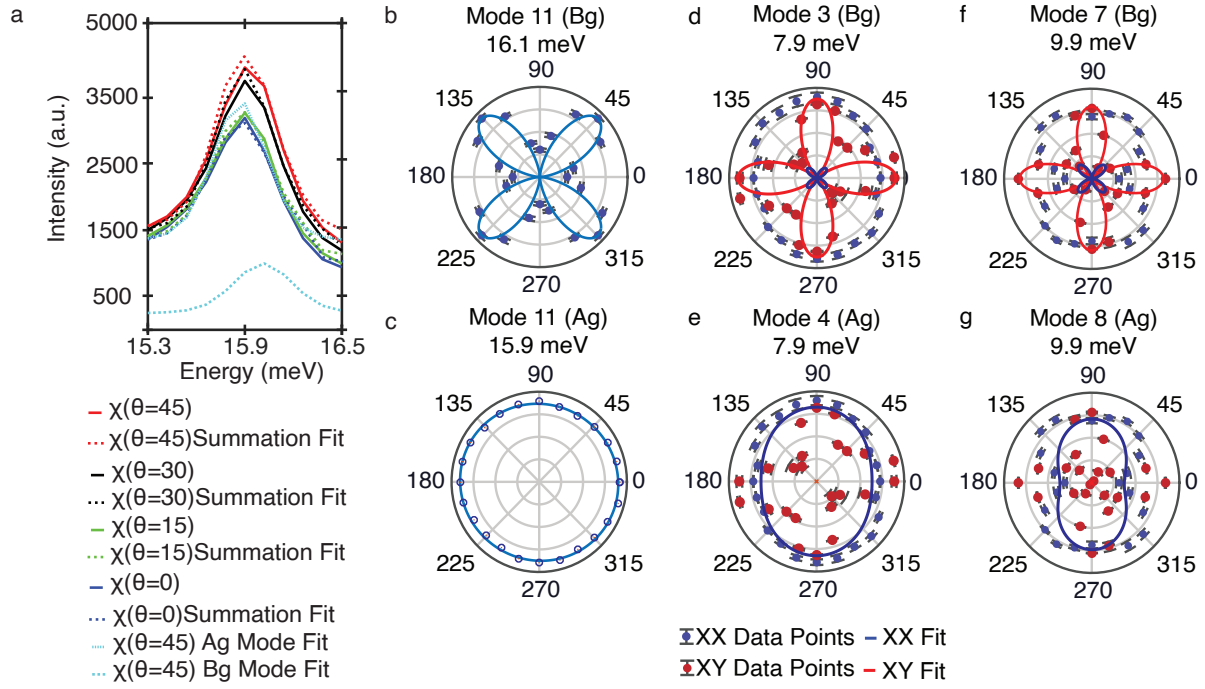

Figure S7: (a) $GdTe_3$ Raman spectra in parallel polarization for polarization angles 0, 15, 30, and 45 degrees (solid lines), near 15.9 meV. Each of these four spectra are accompanied by a summation of the fits for Ag and Bg modes present at 15.9 and 16.1 meV, respectively (dashed lines of same color). This summation is separated into Ag and Bg components for the 45 degree spectrum, shown in the light blue dashed lines. These reveal the presence of nearly degenerate Ag and Bg peaks. (b-c) Experimental results and polar fits for $GdTe_3$ Bg mode at 16.1 meV (b) and Ag mode at 15.9 (c). (d-g) Polar plots of XX(blue dots) and XY(red dots) polarizations for mode 3,4 and 7,8. (d-e) Experimental results and decomposition of the mode at 7.9 meV into degenerate Ag and Bg components, showing accidental overlap of mode 3 and 4. (f-g) Experimental results and decomposition of the mode at 9.9 meV into degenerate Ag and Bg components, showing accidental overlap of mode 7 and 8.

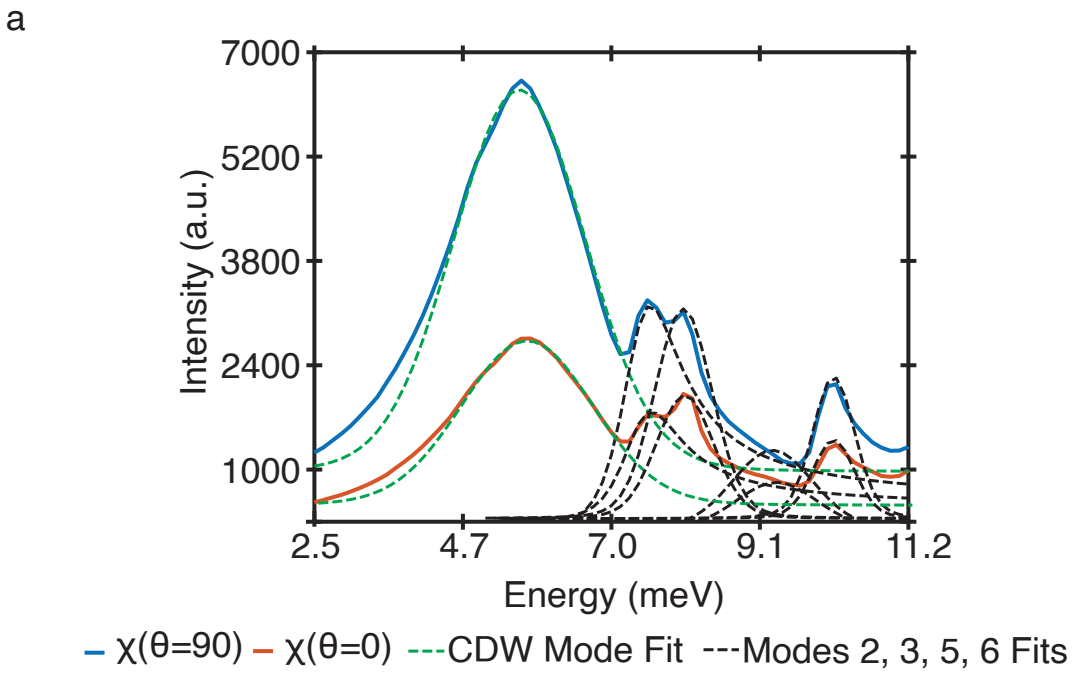

Figure S8: (a) $GdTe_3$ Raman Spectra in parallel polarization for polarization angles of 0 degrees (orange) and 90 degrees (blue). Each spectra is accompanied by fits for individual modes to depict overlap, namely from CDW mode, resulting in Bg symmetry at 9.3 meV being difficult to detect.

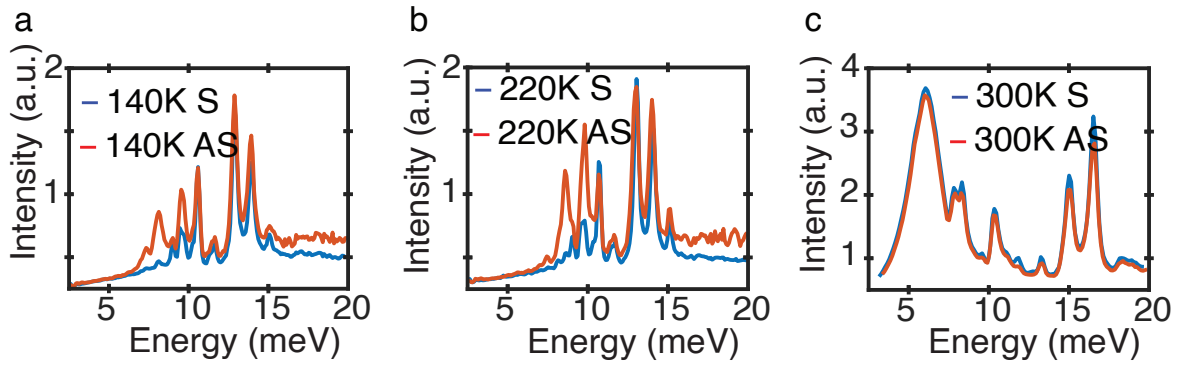

Figure S9: Using calculations from above we would expect equal Raman susceptibility values for both Stokes and anti-Stokes intensity. These plots depict the Stokes (blue) vs. anti-Stokes (orange) Raman susceptibility for $GdTe_3$ (532 nm) at a polarization angle of 165 degrees and temperatures of 140K, 220K, and 300K, going from left to right. As theory suggests, the two susceptibility spectra overlap, with any discrepancies attributed to differences in background input

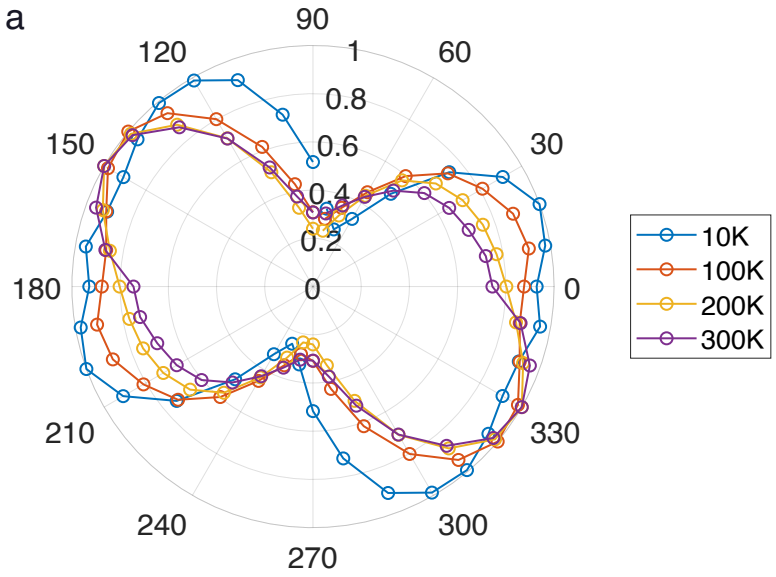

Figure S10: Temperature dependent multidomain cross polarization data

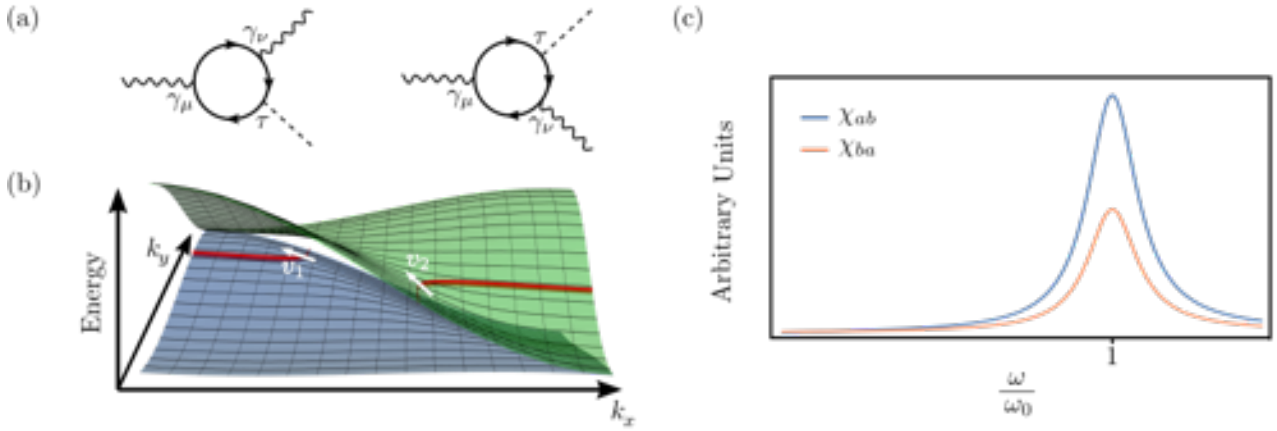

Figure S11: Raman susceptibility. (a) The diagramatic representation of the two processes contributing to resonant Raman scattering. (b) The eigenenergies of the Hamiltonian around one of the points p in the Brillouin zone. The low energy Hamiltonian around the Fermi energy (denoted in red) is given by a linear dispersion with velocities v_1 and v_2, with values depending on the mixing parameters t_3 and t_4. These states are coupled to the opposite region in Brillouin zone where the nesting condition of the CDW is satisfied. (c) The Raman susceptibility as calculated using the low energy model $H_p(\boldsymbol{k})$. The probability of transition shows an asymetry, depending on the chosen pathway. For the calculations in (b) and (c) we have used the representative values $t_1 = 1$, $t_2 = -0.40$, $t_3 = 0.10$, $t_4 = 0.20$, and, $Q = 4\pi/7$. The input frequency and CDW coupling Δ are chosen to be well above the Higg's mode frequency ω_0